nature energy

ARTICLES

https://doi.org/10.1038/s41560-022-01042-5

Check for updates

Hydrogel protection strategy to stabilize water-splitting photoelectrodes

Jeiwan Tan[1,3], Byungjun Kang[2,3], Kyungmin Kim[1], Donyoung Kang[2], Hyungsoo Lee[1], Sunihl Ma[1], Gyumin Jang[1], Hyungsuk Lee[2]✉ and Jooho Moon[1]✉

Photoelectrochemical water splitting is an attractive solar-to-hydrogen pathway. However, the lifetime of photoelectrochemical devices is hampered by severe photocorrosion of semiconductors and instability of co-catalysts. Here we report a strategy for stabilizing photoelectrochemical devices that use a polyacrylamide hydrogel as a highly permeable and transparent device-on-top protector. A hydrogel-protected Sb_2Se_3 photocathode exhibits stability over 100 h, maintaining ~70% of the initial photocurrent, and the degradation rate gradually decreases to the saturation level. The structural stability of a Pt/TiO_2/Sb_2Se_3 photocathode remains unchanged beyond this duration, and effective bubble escape is ensured through the micro gas tunnel formed in the hydrogel to achieve a mechanically stable protector. We demonstrate the versatility of the device-on-top hydrogel protector under a wide electrolyte pH range and by using a SnS photocathode and a $BiVO_4$ photoanode with ~500 h of lifetime.

Cost effective solar-to-hydrogen production has attracted substantial research attention because it provides a pathway to overcome the global reliance on fossil fuels. Photoelectrochemical (PEC) water splitting enables the production of green hydrogen from abundant sunlight and water[1]. The rational design of durable PEC devices is necessary for practical hydrogen production because the fabrication cost and device lifetime influence the overall cost of the system[2,3]. However, ensuring the long-term stability of PEC devices composed of low-cost and earth-abundant materials is challenging as the materials (for example, light-absorbing semiconductors and overlayers) may undergo photocorrosion[4]. Various protection strategies, including TiO_2 deposition by atomic layer deposition (ALD), have been employed to enhance the device stability by physically separating the semiconductors from the electrolyte[5,6]. However, these protective layers cannot be permanently incorporated; for example, surface-accumulated photoelectrons induce self-reduction and dissolution of TiO_2, thereby gradually exposing the inner layer to the corrosive electrolyte[7].

Moreover, the low structural stability of the co-catalyst in a PEC device limits the device lifetime. Although platinum (Pt) exhibits the highest activity towards the hydrogen evolution reaction (HER) and can enhance the photoelectrode performance in terms of the photocurrent and onset potential, instability may be induced owing to the low adhesion of co-catalysts[8]. The detachment of Pt co-catalysts from the TiO_2 protective layer has been frequently observed[9–11]. In general, the performance of PEC devices can be partially recovered after the re-deposition of fresh Pt catalysts; however, the recovered photocurrent density decreases when re-platinization is repeated[11,12]. Inserting a functional layer between the Pt catalyst and protective layer can enhance the interface quality and extend the lifetime of PEC devices to a certain extent[7,13]. Similarly, by replacing the particulate Pt catalyst with an electrodeposited film-type catalyst (for example, RuO_x and MoS_x) that can robustly bind with the bottom layers, the stability of the PEC device can be enhanced compared with that of Pt-decorated counterparts[14,15]. However, the electrodeposition of a co-catalyst requires elaborate control of both the electrolyte and applied potential due to which the photocorrosion of the light-absorbing semiconductor may occur simultaneously. In addition, metal oxide overlayers or membranes, such as SiO_x (ref. [16]), Al_2O_3 (ref. [17]) and TiO_2 (ref. [18]), have been used to encapsulate the as-deposited Pt catalyst to enhance the structural stability of the catalyst by preventing detachment and agglomeration. However, encapsulating the catalyst with solid oxide overlayers typically blocks the catalytic active sites or limits the mass transfer of reactants and products, thereby deteriorating the performance factor. Furthermore, no versatile method has been reported thus far that can prevent both the photocorrosion and physical detachment of the co-catalysts. Consequently, a permanent protection strategy must be formulated for realizing the practical operation of PEC devices[19].

Inspired by photosynthetic marine plants[20–22], we attempted to design a highly permeable and transparent protector for PEC devices. Cells in seaweed are covered by nanoporous hydrogel that can suppress the deformation and rupture of cells caused by physical forces by the aquatic environment[23–25], exhibit a high light transmittance[26] and keep a high water content[27]. Thus, we hypothesized that coating the PEC device with hydrogel can help to enhance performance of the PEC device by ensuring the structural stability. A recent study highlighted that the doctor-blade coating of a thin, porous and superaerophobic virus-based hydrogel on a Si photocathode can increase the photocurrent density by intensifying the bubble detachment[28]. However, the effect of the hydrogel coating in enhancing the long-term stability of the PEC device remains unclear.

Herein, we report a facile protection approach using hydrogel to enhance the stability of PEC devices. Specifically, by employing a cost effective polyacrylamide (PAAM) hydrogel as a device-on-top protector, the lifetime of a reference Pt/TiO_2/Sb_2Se_3 photocathode was substantially high (100 h), and it could maintain ~70% of the initial photocurrent. The hydrogel protector enhanced the structural stability of the Pt catalyst and suppressed the dissolution of

[1]Department of Materials Science and Engineering, Yonsei University, Seoul, Republic of Korea. [2]School of Mechanical Engineering, Yonsei University, Seoul, Republic of Korea. [3]These authors contributed equally: Jeiwan Tan, Byungjun Kang. ✉e-mail: hyungsuk@yonsei.ac.kr; jmoon@yonsei.ac.kr

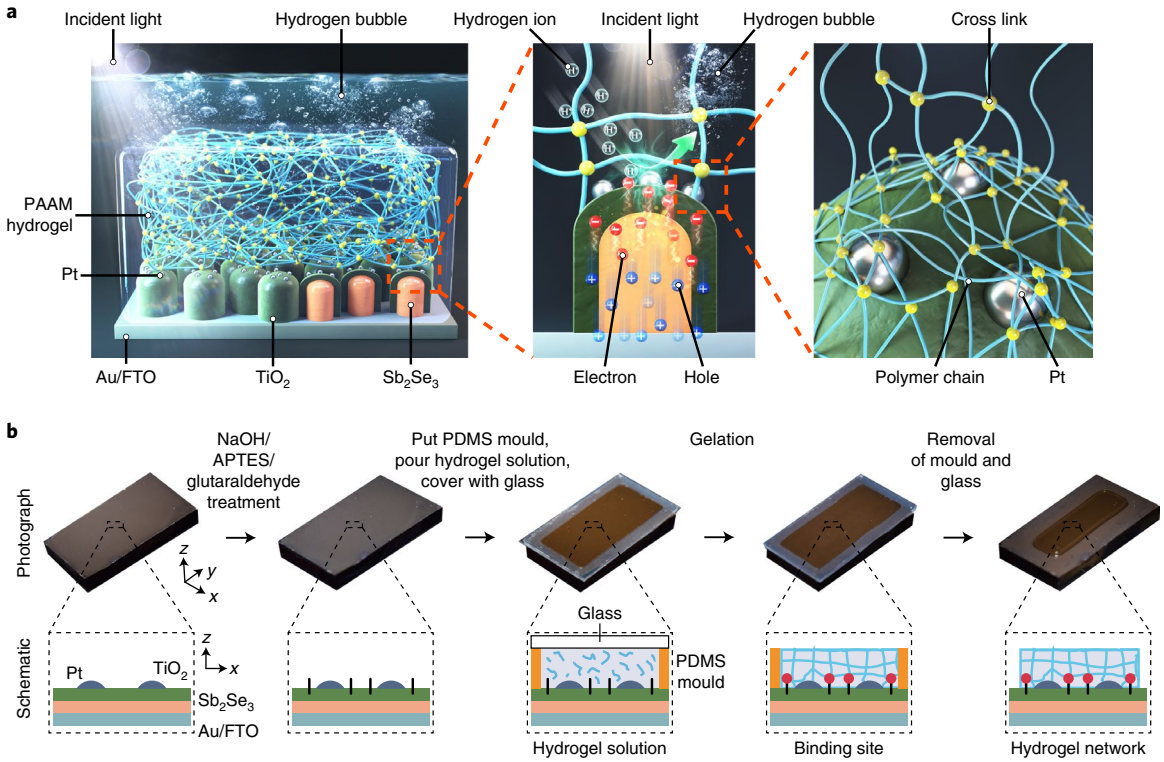

Fig. 1 | Highly permeable and transparent device-on-top hydrogel protector of the PEC device. a, Schematic of PAAM hydrogel-protected Pt/TiO_2/Sb_2Se_3 photocathode for PEC water splitting under illumination. Because the PAAM hydrogel is highly permeable and transparent, hydrogen ions in the electrolyte and incident light can reach the photoelectrode without disturbance from the device-on-top layer. **b**, Fabrication of the device-on-top hydrogel protector. APTES denotes (3-aminopropyl)triethoxysilane.

the TiO_2 layer. The use of the hydrogel protector required the optimization of its mechanical stability, which was controlled by bubble dynamics and physical properties of the hydrogel, such as thickness and concentration.

Fabrication of PAAM hydrogel protector

As the light absorber, we employed Sb_2Se_3, which is an emerging low-cost semiconductor for photovoltaic[29–31] and PEC devices[7,8]. The TiO_2 overlayer contributes to physical protection and *p*–*n* heterojunction formation, whereas the surface-decorated Pt nanoparticles function as the HER catalyst with negligible overpotential[7,8]. In general, a device-on-top protector must be transparent to sunlight, chemically inert to the electrolyte and highly permeable to water. Prescreening tests were conducted for hydrogel candidates, and PAAM was selected as a protector owing to its high transmittance and chemical inertness without decomposition in a H_2SO_4 electrolyte (Supplementary Fig. 1). The volumetric water content of the PAAM hydrogel in our experimental condition was higher than 85% (Supplementary Fig. 2). Owing to the high water volume fraction, it is expected that the ion concentration in the gel would be similar to that in the electrolyte outside the hydrogel[32]. The PAAM hydrogel (monomer concentration = 10%) was applied to a reference Sb_2Se_3 photocathode (that is, Pt/TiO_2/Sb_2Se_3/Au/fluorine-doped tine oxide (FTO)/soda-lime glass; Fig. 1a) using the mould-casting technique (Fig. 1b)[33]. Polydimethylsiloxane (PDMS) moulds were used to regulate the thickness of PAAM on the surface-treated device.

PEC profiles

The PEC characteristics of photocathodes with and without the hydrogel protector (denoted as PAAM and No PAAM, respectively) are shown in Fig. 2. Typically, there exists a trade-off between the PEC device performance and use of the device-on-top protector, as it may block the catalytically active sites. However, when the hydrogel coating was applied, the photocurrent density (J_{ph}) at 0 V versus reversible hydrogen electrode (V_{RHE}) increased from 16 mA cm^{-2} to 19 mA cm^{-2}, whereas the onset potential did not exhibit any substantial variation (Fig. 2a). Compared with No PAAM, the light absorption of PAAM increased by only ~2% over the entire wavelength range (Supplementary Fig. 3). Thus, the increase of ~15% in J_{ph} probably originated from the enhanced quantum efficiency rather than the optical effect. Considering the similar charge transport properties in both devices owing to the identical Pt/TiO_2/Sb_2Se_3 structure, the enhanced J_{ph} could be attributed to the higher surface charge transfer efficiency. According to an existing study on superaerophobic hydrogels[28], hydrogel coatings enlarge the active sites during the PEC operation by suppressing the bubble growth along the device surface, rather than enhancing the catalytic activity (Supplementary Note 1). Moreover, the PAAM hydrogel is an aerophobic hydrogel owing to its high hydrophilicity, indicated by a low water contact angle of ~8.2° (refs. [34,35]).

The incident photon-to-current conversion efficiency (IPCE) spectra indicated enhanced harvesting of long-wavelength photons for PAAM, and the integrated IPCE values for both the devices, based on the solar air mass (AM) 1.5 spectrum, matched the experimentally measured J_{ph} values (Fig. 2b). In the case of No PAAM, although surface bubbles blocked the photoelectrons generated near the surface through the absorption of short-wavelength photons (that is, high-energy photons), the photoelectrons still participated in the HER before surface recombination occurred because the diffusion length was sufficiently larger than the travelling distance. However, because the longer-wavelength photons generally penetrated deeper into the absorber layer, leading to an increased

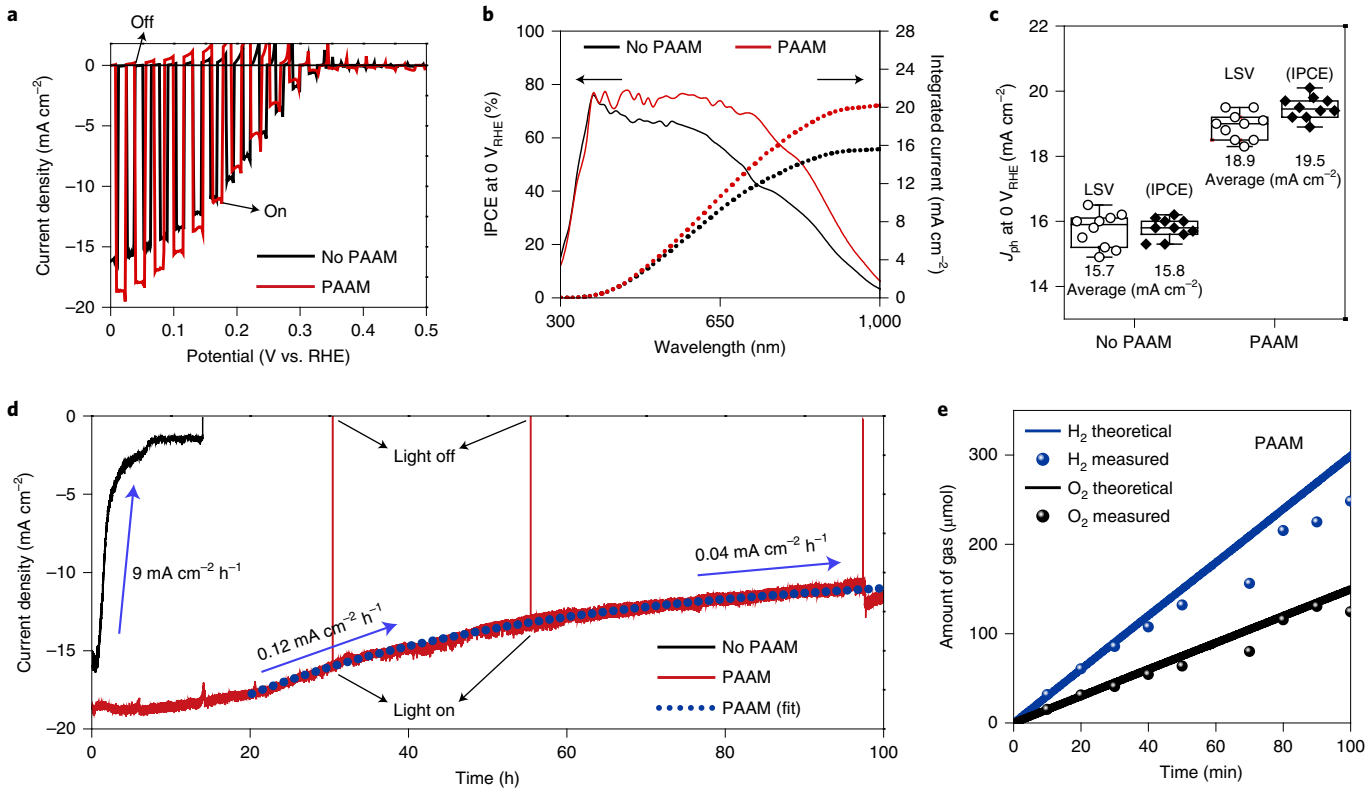

Fig. 2 | PEC characteristics of the Sb_2Se_3 photocathodes with and without the device-on-top hydrogel protector. a,**b**, Photocurrent density–potential curve (**a**) and incident photon-to-current conversion efficiency (IPCE) spectra at 0 V_{RHE} (**b**) for No PAAM and PAAM in a H_2SO_4 electrolyte (pH = 1). **c**, Performance reproducibility and average J_{ph} at 0 V_{RHE} of both devices (n = 10 for each). A bottom-, centre- and top-bound of box represents the 25th, 50th and 75th percentiles, respectively. Whiskers of boxes represent the minima and maxima. LSV denotes linear sweep voltammetry. **d**, Time-dependent current density of both devices measured at 0 V_{RHE} via chronoamperometry. The blue arrows indicate the J_{ph} degradation rate, as calculated in Supplementary Fig. 4. **e**, Hydrogen and oxygen production as a function of the operating time during stability testing of PAAM. The solid line represents the ideal curve calculated for 100% Faradaic efficiency, whereas the circles indicate the values quantified through a gas chromatography analysis. The monomer concentration of the hydrogel is 10%.

travelling distance of the photoelectrons, the surface recombination became dominant if the active sites were blocked by the bubbles. In contrast, the notable IPCE enhancement of PAAM for the long-wavelength photons indicated that the large amount of photoelectrons generated far from the surface could effectively participate in the HER, which is essential for the bottom electrode in tandem devices. The performance reproducibility of both photocathodes was confirmed by obtaining the linear sweep voltammetry (LSV) curves and IPCE values for ten devices; the average J_{ph} at 0 V_{RHE} was 15.7 mA cm^{-2} and 18.9 mA cm^{-2} for No PAAM and PAAM, respectively (Fig. 2c).

Stability of PEC devices

Interestingly, by employing the device-on-top hydrogel protector, the lifetime of the Sb_2Se_3 photocathode was extended remarkably, as shown in Fig. 2d. PAAM exhibited stable operation over 100 h, maintaining ~70% of the initial J_{ph} (J_o), whereas No PAAM exhibited rapid photocurrent degradation and was completely damaged within 5 h. This finding was in agreement with that observed in our previous study[7]. Before any abrupt photocurrent degradation (<1 h for No PAAM), our hydrogel-protected Sb_2Se_3 photocathode exhibited a 100 times higher stability. The amounts of H_2 and O_2 gas produced during stable operation were quantified through a gas chromatography analysis (Fig. 2e). The molar ratio of H_2 and O_2 was approximately 2:1, consistent with the theoretically calculated value, and the Faradaic efficiency ranged from 80% to 100%, implying that a reasonable amount of hydrogen gas escaped from the hydrogel protector. The fluctuation of J_{ph}, attributable to the repeated cycles of current reduction through bubble generation and current recovery through bubble detachment, is discussed in Supplementary Note 2. Supplementary Fig. 4 shows the J_{ph}/J_o value and J_{ph} degradation rate as a function of the operation duration. In the case of No PAAM, the degradation rate increased rapidly up to 9 mA cm^{-2} h^{-1} (at 1.5 h), decreasing J_{ph} to ~60% of J_o. In contrast, the degradation rate of PAAM was low (maximum 0.12 mA cm^{-2} h^{-1}) and gradually decreased when the value nearly saturated at J_{ph} ~12 mA cm^{-2} after 100 h.

The PEC performance and stability values of existing low-cost solution-processed thin film photocathodes, including Cu_2O, Sb_2Se_3 and Cu-kesterites, are summarized in Supplementary Table 1. Most photocathodes involving the Pt co-catalyst exhibit a relatively low stability (<10 h), probably because of the detachment. To the best of our knowledge, only one low-cost semiconductor-based photocathode (that is, NiMo/TiO_2/Ga_2O_3/Cu_2O) of this type exhibits stable operation beyond 100 h; however, J_{ph} is only ~6 mA cm^{-2}, and the photocurrent degradation rate gradually increases after ~80 h (ref. [36]). Furthermore, the state-of-the-art Si photocathodes with developmental maturity exhibit a high photocurrent density and stability, and several researchers have reported stable operation for more than 1,000 h (Supplementary Table 2). However, Si wafer-based devices include either an expensive and complicated fabrication process for surface nanostructuring/doping, sophisticated device structure or high-temperature annealing, which are not generally applicable to low-cost solution-processed thin film photocathodes. Although catalyst-encapsulating strategies using ~10 nm thin

solid oxide overlayers (*for* example, SiO_x membranes, Al_2O_3, or ALD-TiO_2)[16–18] have been formulated to enhance the device stability, the diffusivity of reactants and products inside the solid severely decreases compared with that in the liquid, which deteriorates the performance factors. Therefore, thus far, only 'thin' oxide layers have been used as device-on-top protectors, although they cannot be applied to sophisticated nanostructured photoelectrodes because of non-uniformity and delamination issues. For example, when an ALD-TiO_2 overlayer was applied to a nanostructured Pt/TiO_2/Sb_2Se_3 photocathode, the device lifetime could be extended to ~10 h (J_o = 13.8 mA cm^{-2}, J_{ph}/J_o < 20 %, Supplementary Fig. 5), although this enhancement was less than that achieved using the hydrogel protecting strategy. Notably, the proposed hydrogel protector is highly transparent and permeable, with a water content of ~90%. Therefore, this protector can be used as a device-on-top framework for PEC devices and can be easily applied to nanostructured surfaces without thickness limitations.

In most existing studies, the stability of PEC devices has been evaluated considering only the duration of stable operation or J_{ph}/J_o after this duration. However, from a practical viewpoint, the final degradation rate must be considered to predict the expected real lifetime. When J_{ph} begins to decrease, the degradation occurs more rapidly because detachment of the catalyst and severe photocorrosion of the semiconductor occur simultaneously[37]. Surprisingly, in our research, PAAM demonstrated a stability with a substantially high J_{ph} among various low-cost thin film photocathodes, and the degradation rate of J_{ph} gradually decreased. By simply extrapolating the J_{ph}–time curve of PAAM using an exponential function (Fig. 2d), we obtained a saturated J_{ph} of ~9 mA cm^{-2} over 1,000 h. This assumption is reasonable when the structural stability of the Pt catalyst and TiO_2 layer (that is, without the reductive dissolution) and mechanical stability of the device-on-top hydrogel protector have been ensured.

Structural stability of PEC devices

The surface scanning electron microscopy (SEM) images for No PAAM as a function of J_{ph}/J_o during the PEC operation are shown in Supplementary Fig. 6a. The rod-shaped microstructure was maintained until J_{ph}/J_o reached ~70%, whereas the diameters of individual rods decreased after J_{ph}/J_o < 50%, owing to TiO_2 dissolution, as observed in our previous study[7]. To investigate the structural variations of the Pt catalyst, before the severe dissolution of TiO_2, transmission electron microscopy (TEM) was performed on the cross-sectioned samples of an as-prepared Sb_2Se_3 photocathode, No PAAM and PAAM after PEC operation until J_{ph}/J_o became ~70% (Fig. 3a–f). Uniform Pt nanoparticles were observed on the TiO_2 layer of the as-prepared Sb_2Se_3 photocathode. However, when J_{ph}/J_o decreased to 70%, agglomeration and partial detachment of the Pt catalysts were clearly observed for No PAAM. According to previous studies, the mechanical stress induced by the hydrogen bubble growth on the Pt surface drives the migration and agglomeration of the Pt nanoparticles, which severely degrades the HER performance[38]. Notably, PAAM exhibited well-attached Pt catalysts without any severe agglomeration, even after ~100 h, although the thickness of the Pt nanoparticle layer slightly decreased, leading to a ~30% decrease in the photocurrent. The enhanced structural stability of the Pt catalyst could be attributed to the spatial confinement imposed by the nanoporous network of the PAAM hydrogel[39,40] (Fig. 3g and Supplementary Fig. 7). Although Jeon et al. observed that a microporous hydrogel network enables rapid bubble detachment, the authors focused only on the J_{ph} improvement under a highly negative potential region (−0.9 V_{RHE}), achieved by preserving the active sites without considering the structural stability of the Pt catalyst[28]. Moreover, supplying the surfactant in an electrolyte allowed rapid bubble detachment and prevented the formation of large bubbles; however, this strategy barely enhanced the lifetime of No PAAM (Supplementary Fig. 8). In this context, the role of the hydrogel as a 'protector' that substantially extends the lifetime of the PEC device remains to be explored.

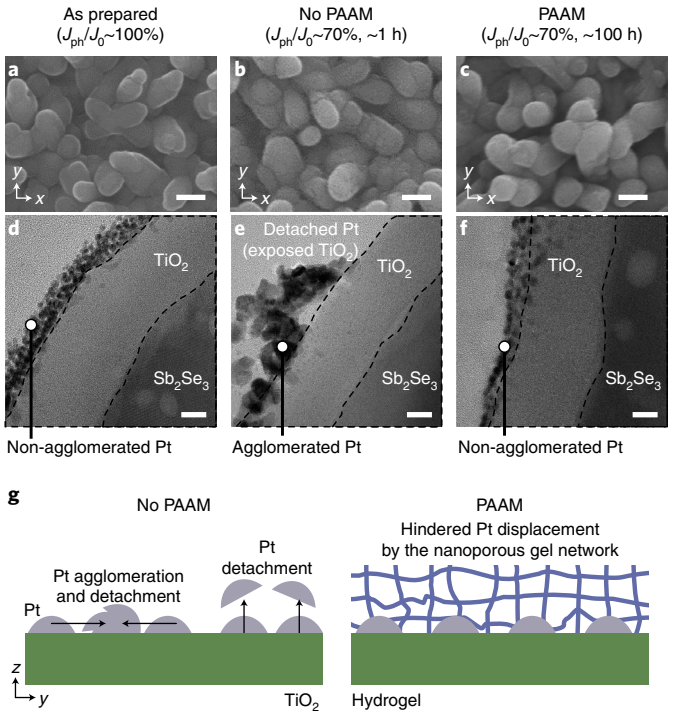

Fig. 3 | Enhancement of catalyst stability by the device-on-top hydrogel protector. a–f, Surface SEM images (**a–c**) and cross-sectional TEM images (**d–f**) of the as-prepared Sb_2Se_3 photocathode (J_{ph}/J_o ~100%) (**a** and **d**), No PAAM (J_{ph}/J_o ~70%, ~1 h) (**b** and **e**) and PAAM (J_{ph}/J_o ~70%, ~100 h) (**c** and **f**). The Pt nanoparticles are agglomerated and detached from the TiO_2 surface only in the case of No PAAM. The scale bars for **a–c** and **d–f** represent 200 nm and 10 nm, respectively. **g**, Schematic of the Pt confinement effect by the device-on-top protector.

Owing to Pt agglomeration and detachment, some parts of the TiO_2 layer are directly exposed to the electrolyte, where the surface charge transfer rate towards the HER becomes sluggish. The accumulated photoelectrons then reduce the TiO_2 surface instead of generating hydrogen, followed by dissolution into the surrounding electrolyte in the form of Ti^{3+} ions[7]. Although the surface morphologies observed in the SEM images were similar until J_{ph}/J_o ~70%, dissolution of the TiO_2 layer was observed in the scanning transmission electron microscopy (STEM) and energy-dispersive X-ray spectroscopy (EDS) analyses performed on the representative cross-sectioned samples (Fig. 4a and Supplementary Fig. 6b–e). In the case of No PAAM, the thickness of TiO_2 decreased by ~5 nm when J_{ph}/J_o was 70% after ~1 h (Fig. 4b). Interestingly, only ~1.2 nm of TiO_2 dissolved even after ~100 h in the case of PAAM. The high degradation rate for No PAAM was attributable to the Pt agglomeration and immediate dissolution of the exposed region of TiO_2 (Supplementary Fig. 4). In contrast, the spatial confinement effect of the Pt catalyst by the hydrogel minimized the direct exposure of TiO_2; thus, the degradation rate for PAAM was ~100 times smaller. Even though ~1.2 nm of the TiO_2 layer of PAAM dissolved, any additional dissolution was suppressed, evidenced by the gradually decreasing degradation rate of J_{ph}.

The diffusivity of the metal cations in the PAAM hydrogel (D^{gel}) has been noted to be 60–100% lower than that in the electrolyte solution ($D^{solution}$) because of the steric and electrostatic interactions between the hydrogel network and metal ions[41]. That is, although Pt is not completely confined and partial dissolution of TiO_2 occurs (~1.2 nm), the dissolved Ti^{3+} ions can be temporarily

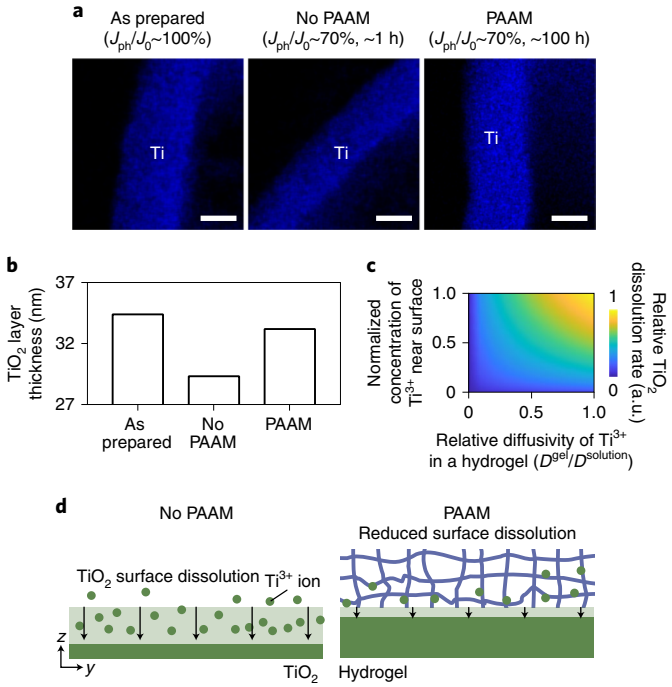

Fig. 4 | Suppression of TiO_2 photocorrosion by the device-on-top hydrogel protector. a,**b**, Ti elemental mapping by STEM-EDS (**a**) and average thickness of TiO_2 layer (**b**) of the as-prepared Sb_2Se_3 photocathode (J_{ph}/J_o ~100%), No PAAM (J_{ph}/J_o ~70%, ~1h) and PAAM (J_{ph}/J_o ~70%, ~100 h) estimated from the height profile shown in Supplementary Note 3. Scale bars represent 20 nm. **c**, Calculated relative TiO_2 dissolution rate as a function of the normalized concentration of Ti^{3+} near the surface and relative diffusivity of Ti^{3+} in a hydrogel. **d**, Schematic of TiO_2 protection by the device-on-top hydrogel protector. The monomer concentration of the hydrogel is 10%.

stagnant inside the hydrogel network. Consequently, the dissolved Ti^{3+} concentration inside the hydrogel is expected to increase during the PEC operation, thereby suppressing the additional dissolution of TiO_2, according to Le Chatelier's principle. To clarify this phenomenon, we theoretically calculated the TiO_2 dissolution rate based on the corrosion model suggested by Schiner and Hellmich[42] (Supplementary Note 4). When the hydrogel protector was used, the accumulation of the photoelectrons that reduced the TiO_2 surface was strongly inhibited (that is, a low normalized Ti^{3+} concentration was observed at the TiO_2 surface before the dissolution); and the reduced relative diffusivity ($D^{gel}/D^{solution}$) of the dissolved Ti^{3+} ions inside the hydrogel synergistically decreased the TiO_2 dissolution rate (Fig. 4c). These observations were supported by the inductively coupled plasma mass spectroscopy (ICP-MS) analysis, which helped clarify the dissolved metallic species in the used electrolyte as a function of the duration. When the PEC device was operated, the Ti concentration increased in the case of No PAAM, whereas almost no variation was observed for PAAM. Instead, ~30 times higher concentration of Ti was detected inside the mechanically detached hydrogel protector after ~100 h (Supplementary Fig. 9). Therefore, the device-on-top protector provided both physical and chemical barriers to maintain the structural integrity of the PEC device (Figs. 3g and 4d).

Mechanical stability of the hydrogel protector

In addition to the structural stability of the Pt catalyst and TiO_2 layer, the mechanical stability of the device-on-top hydrogel protector is critical for ensuring long-term operation of the PEC device. To determine the effect of the hydrogel monomer concentration on the device stability, we performed experiments in which the concentrations of hydrogel protectors with a constant thickness of 400 µm were varied. For the 400 µm-thick hydrogel protector with a monomer concentration of 6% and 30% (denoted as 6% PAAM and 30% PAAM, respectively), J_{ph} remained stable in the initial 4 h (Fig. 5a), indicating that the surface structure of the Pt catalyst was well maintained. However, after 4 h, the 6% and 30% PAAM exhibited different degradation characteristics. First, J_{ph} decreased, with J_{ph}/J_o ~20% for 6% PAAM. Visualization of the bubble dynamics indicated that the sudden decrease in J_{ph} for 6% PAAM was attributable to the bubbles trapped in the hydrogel, which expanded to cover the entire area of the PEC surface (Fig. 5b). However, the $Pt/TiO_2/Sb_2Se_3$ microstructure of the photocathode was preserved even when J_{ph}/J_o ~20% (Supplementary Fig. 10a,b). We observed the partial recovery of J_{ph} by manually bursting the bubble covering the surface (Fig. 5a). The decrease in the photocurrent for 6% PAAM could be attributed to the bubbles hindering the PEC operation instead of the structural degradation of the Sb_2Se_3 photocathode. In contrast, for 30% PAAM, J_{ph} continuously decreased over tens of hours with a degradation rate higher than 10% PAAM (that is, J_{ph} did not saturate). Although bubbles were clearly observed in the case of 6% and 10% PAAM (Fig. 5b,c), bubbles were not clearly observed (the bubbles were non-spherical) at J_{ph}/J_o ~80% in the case of 30% PAAM, indicative of hydrogel fractures (Fig. 5d; magnified images are shown in Supplementary Fig. 11). According to the theoretical analysis, the fracture probability, defined as the ratio of the maximum pressure (P_{max}) applied to the hydrogel by a bubble to the critical fracture pressure (P_f) (ref. [43]), increased with the hydrogel volume fraction (Fig. 5e and Supplementary Note 5). According to the STEM-EDS analysis, extensive detachment of the Pt catalyst and dissolution of TiO_2 occurred at J_{ph}/J_o ~20% in the case of the 30% PAAM (Supplementary Fig. 10c). The results suggest that the J_{ph} degradation depends on the spatial confinement, which is influenced by the monomer concentration of the hydrogel in the PEC device.

Furthermore, we investigated the influence of the thickness of the hydrogel protector on the device stability by performing experiments and computational simulations with hydrogels with different thicknesses and a constant monomer concentration of 10%. Hydrogel protectors thinner and thicker than 400 µm were categorized as 'thin hydrogel protectors' and 'thick hydrogel protectors', respectively. The J_{ph} values of devices with thin hydrogel protectors (thickness of 50 µm, 100 µm and 200 µm) substantially decreased within a few hours, similar to No PAAM (Fig. 6a). The device lifetime of thick hydrogel protectors (thickness of 600 µm, 800 µm and 1,200 µm) was substantially higher than that of the thin hydrogel protectors, and the photocurrent degradation rate increased with the hydrogel thickness (Fig. 6b). To clarify the mechanical behaviour of the hydrogel protector with an embedded growing bubble as a function of the hydrogel thickness, we conducted a computational analysis via finite element modelling (Supplementary Video 1). In the case of a thin hydrogel, the Von Mises stress generated inside the hydrogel during the bubble growth was higher than that for a thick hydrogel (Fig. 6c). Owing to the comparable dimension of the hydrogel relative to the bubble size, nearly the entire area of the hydrogel was subjected to mechanical stress. This result indicates that the protective role of the hydrogel, in providing spatial confinement over the device surface, might be diminished in the case of the thin hydrogel protector. Local delamination of the thin hydrogel protector was observed at J_{ph}/J_o ~80%, and the device surface exhibited a dark ash colour at J_{ph}/J_o ~20%, indicating structural degradation of the Sb_2Se_3 photocathode with a thin hydrogel protector (Fig. 6d and Supplementary Fig. 12). The SEM image confirmed that the morphology of rod-shaped Sb_2Se_3 photocathodes with thin hydrogel protectors was substantially degraded at J_{ph}/J_o ~20%

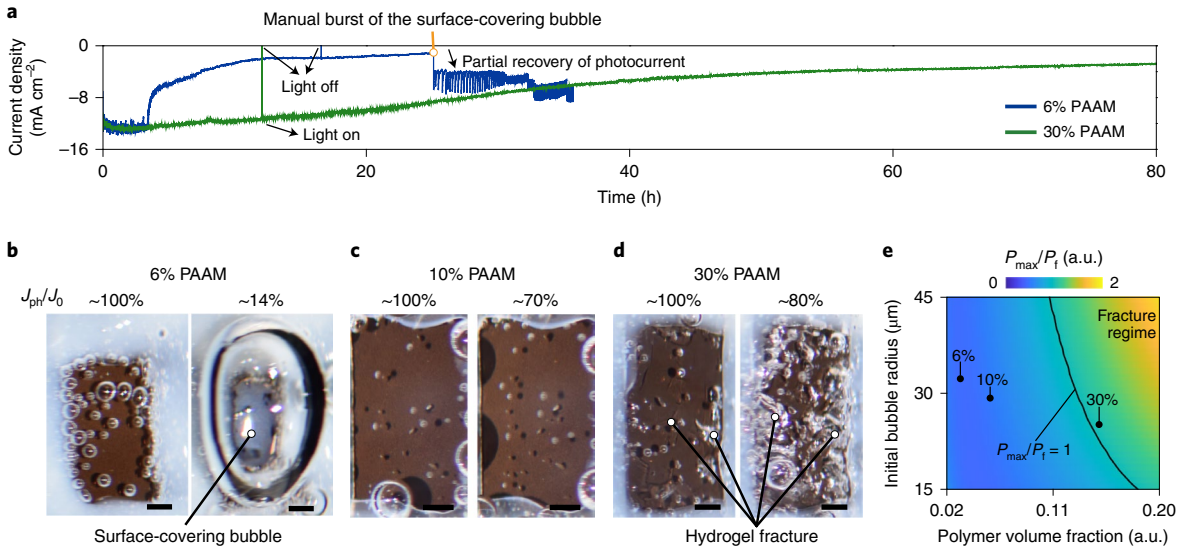

Fig. 5 | Effect of PAAM monomer concentration on the bubble dynamics in the device-on-top hydrogel protector. a, Time-dependent current density of Sb_2Se_3 photocathodes with 6% and 30% PAAM hydrogel protector. **b**–**d**, Photographs of 6%, 10% and 30% PAAM during PEC operation: (b) generation of the surface-covering bubble inside 6% PAAM (**b**); effective bubble escape from the 10% PAAM (**c**); fractured hydrogel protector during operation of 30% PAAM (**d**). **e**, Ratio of the maximum pressure applied on the hydrogel by the bubble growth (P_{max}) to the critical pressure for fracture (P_f) as a function of the polymer volume fraction and initial bubble radius. The regime of hydrogel fracture is delineated by a line representing $P_{max}/P_f = 1$. The thickness of the hydrogel layer is 400 μm. Scale bars represent 1 mm.

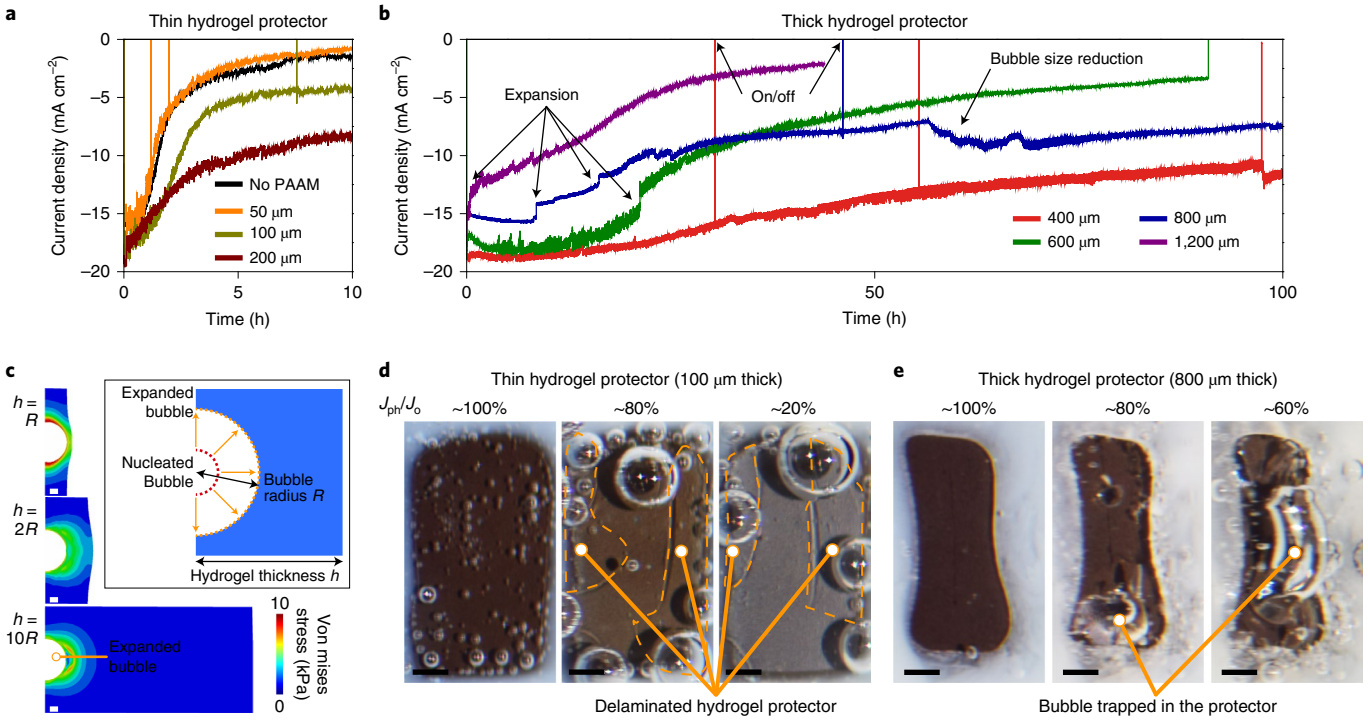

Fig. 6 | Effect of hydrogel thickness on the bubble dynamics in the device-on-top hydrogel protector. a,**b**, Time-dependent current density of the photocathodes with thin (<400 μm) (**a**) and thick (<400 μm) (**b**) hydrogel protector. **c**, Finite element modelling to investigate the effect of hydrogel thickness on the Von Mises stress distribution during the bubble growth. The hydrogel thicknesses (h) are 1, 2, and 10 times the final radius of the bubble (R). The scale bar represents 20 μm. **d**,**e**, Representative photographs of photocathodes with thin (**d**) and thick (**e**) hydrogel protectors. Local delamination of the 100 μm-thick hydrogel protector is delineated by the orange dotted lines. The scale bar represents 1 mm. The monomer concentration of the hydrogel is 10%.

(Supplementary Fig. 13a). The microstructure of the Sb_2Se_3 photocathodes with the thick hydrogels remained intact even at J_{ph}/J_o ~20% (Supplementary Fig. 13b and 13c). This result suggests that the J_{ph} degradation in the case of thick hydrogel protectors could be attributed to the altered bubble dynamics rather than structural degradation of the device.

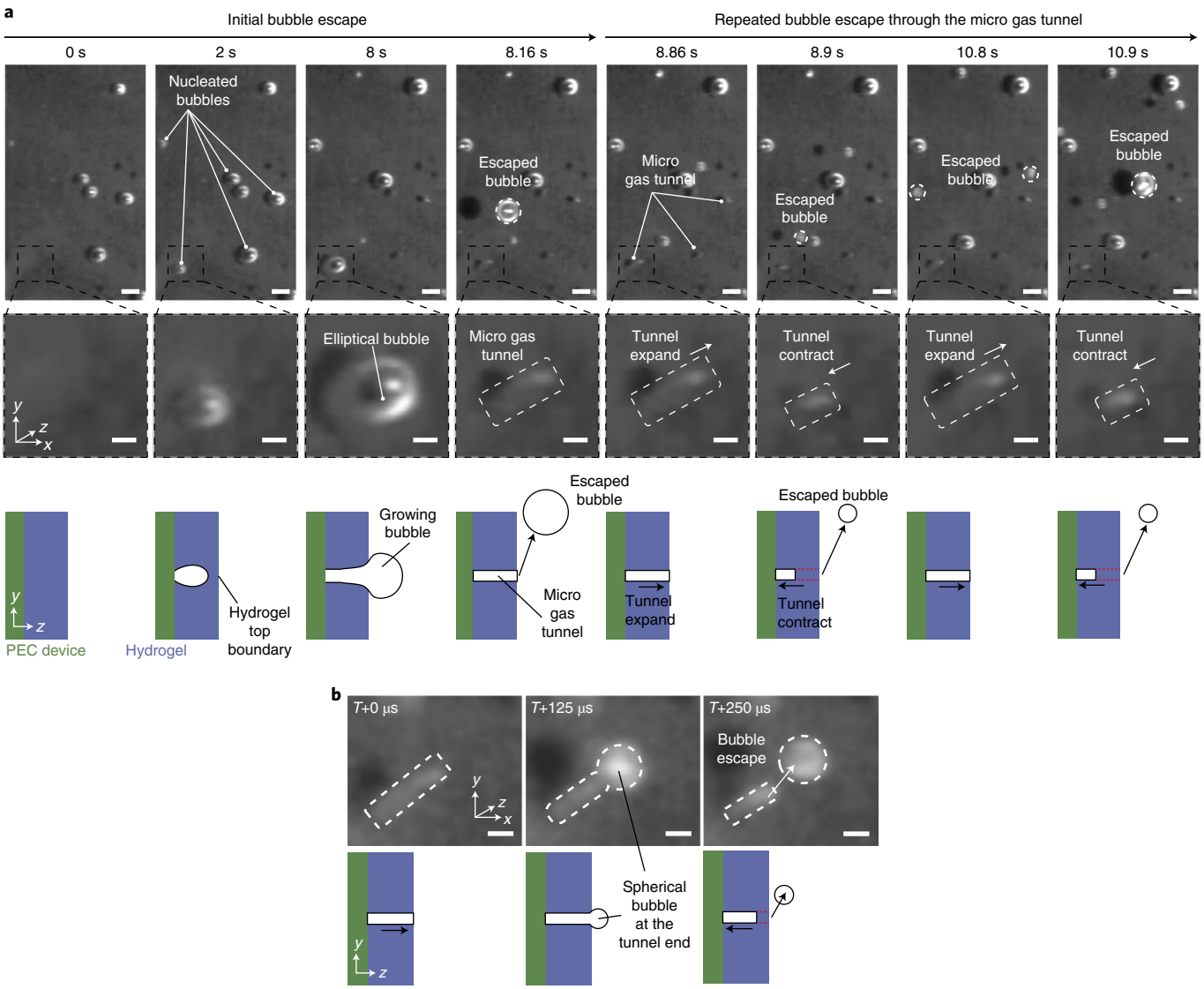

Fig. 7 | Generation and effective escape of the hydrogen bubble through the micro gas tunnel formed in the device-on-top hydrogel protector. **a**, Non-magnified (first row) and magnified (second row) images of bubbles on the device surface. The *y*–*z* cross-sectional schematics (third row) illustrate the nucleation and growth of hydrogen bubble in the protector and bubble escape from the protector for 10% PAAM. Scale bars in the first and second rows represent 300 μm and 100 μm, respectively. **b**, High-speed images of the bubble escape at the end of the micro gas tunnel. The boundaries of the bubble are represented by white dotted lines. Scale bars represent 100 μm.

Notably, the bubble dynamics play a key role in J_{ph} degradation by controlling the light scattering and electrolyte mass transfer. The scattering of light incident to the device surface can be limited by the bubbles. J_{ph} may decrease owing to the reduced photoelectron generation because of the optical loss. Furthermore, if the electrolyte mass transfer is hindered by trapped bubbles, the HER at the Pt catalyst may become sluggish. Consequently, photoelectrons may accumulate at the device surface, inducing the reductive dissolution of TiO_2. According to the results of 400 μm-thick 6% PAAM and 800 μm-thick 10% PAAM, in which relatively large trapped bubbles were observed (Figs. 5b and 6e), J_{ph} decreased without TiO_2 dissolution. This finding implies that the J_{ph} degradation was attributable to the variation in the bubble dynamics with the thickness values and concentrations of the hydrogel protector.

Bubble dynamics in the hydrogel protector

To clarify the bubble dynamics, we monitored the nucleation, growth and escape of bubbles in situ for the 400 μm-thick 10% PAAM protector during PEC operation by using a high-speed camera. Bubbles nucleated inside the hydrogel and expanded in an elliptical shape while being displaced towards the hydrogel surface, as observed at <8 s in Fig. 7a and Supplementary Video 2. The mechanical stress generated locally near the expanding bubbles probably led to the deformation of the hydrogel structure including the pores. When bubbles reached the top surface of the hydrogel, they probably escaped through the enlarged pores, as observed at 8.16 s in Fig. 7a. At the tip of the tunnel, the bubbles became spherical upon escaping. The escaped bubbles detached within 250 μs (Fig. 7b). Newly produced bubbles appeared to escape following the same trajectory periodically, indicating that a microscale tunnel formed for bubble transfer inside the hydrogel.

As the thickness of the hydrogel increased, the strain energy required for a bubble to escape from the hydrogel increased, and bubbles tended to be trapped. Large bubbles could be formed through the expansion or coalescence of trapped bubbles, as observed in 10% PAAM with a thick protector (Fig. 6e). Owing to

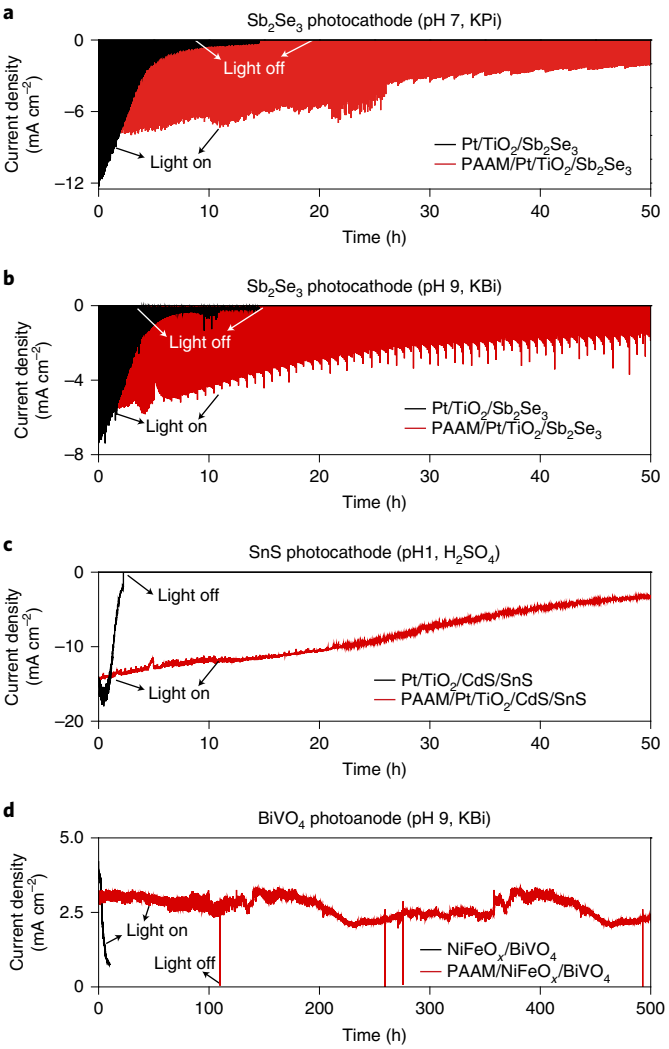

Fig. 8 | Versatility of the device-on-top hydrogel protector. The stability of various photoelectrodes with and without the device-on-top protector is characterized under a wide pH range. **a**,**b**, Sb_2Se_3 photocathodes with neutral (pH 7, KPi) (**a**) and basic (pH 9, KBi) (**b**) electrolytes. **c**, SnS photocathode with acidic electrolyte (pH 1, H_2SO_4). **d**, $BiVO_4$ photoanodes with basic (pH 9, KBi) electrolyte. The monomer concentration of the hydrogel is 10%. The thickness of the hydrogel protector is 400 μm for **a**,**b** and **c** and 800 μm for **d**. Chronoamperometry is performed under automatic light chopping for **a** and **b** (on/off = 10/10 s) and continuous illumination with manual shutdown for **c** and **d** (off interval = 1 min).

the poroelastic property of the hydrogel[44], chemical properties such as the water content, the microstructure, mechanical properties and the thickness of the hydrogel protector considerably influenced the photocurrent degradation by regulating the bubble dynamics. The lifetime of PEC devices could likely be enhanced by engineering chemical and mechanical properties of the hydrogel protector.

Our results indicate that the produced hydrogen gas molecules in the device-on-top protector exhibited more regulated dynamics when they were nucleated and escaped through the gas tunnel, compared with the irregular movement of bubbles observed at the device surface without the protector. In the case of No PAAM, the bubbles grew and translated upward, resulting in shear stress on the surface of the photocathode, which decreased the structural stability of the Pt catalyst (Supplementary Fig. 14 and Supplementary Video 3). In the case of PAAM, the hydrogel protector confined the lateral displacement of the bubbles, thereby preventing shear stress generation on the surface, which can help maintain the structural stability of Pt catalysts, as observed in Fig. 3.

Versatility of the hydrogel protector

The versatility of the device-on-top hydrogel protector was evaluated under a wide pH window of the electrolyte and by using a low-cost thin film SnS photocathode and a $BiVO_4$ photoanode (Fig. 8). The PAAM device could be operated in neutral (pH 7, potassium phosphate buffer (KPi)) and basic (pH 9, potassium borate buffer (KBi)) conditions for over 50 h (Fig. 8a,b), although the initial J_{ph} was reduced compared with No PAAM, and J_{ph} fluctuation was frequently observed during PEC operation. The PAAM (400 μm)/Pt/TiO_2/CdS/SnS photocathode operated for a period more than 50 times larger than that of the unprotected counterpart under an acidic electrolyte (pH 1, H_2SO_4) without notable J_{ph} fluctuation (Fig. 8c). Because J_{ph} fluctuation was observed when bubbles trapped inside the hydrogel expanded/contracted, we speculated that the dissolved metal cations (for example, Na^+ and K^+) in buffered electrolytes probably interacted with the hydrogel networks during PEC operation, inhibiting effective bubble escape from the hydrogel. The low value of initial J_{ph} for PAAM-protected PEC devices, which might be also influenced by metal cations, may lead to the less degradation rate of the photocurrent. Nevertheless, the surface microstructure of these photocathodes was well maintained even after the stability test (Supplementary Fig. 15), demonstrating the protection role of hydrogel during PEC operation.

Typically, state-of-the-art Si photocathodes exhibit relatively longer lifetimes than the solution-processed thin film-type photocathodes (Supplementary Table 2). Excluding the high-level strategies that are applicable only on Si wafer, a reference TiO_2(3 nm)/Pt/TiO_2/*p*-Si photocathode showed rapid photocurrent degradation within 10 h ($J_{ph}/J_{ph,max}$ ~10% after the test). We also prepared a hydrogel-protected Si photocathode counterpart, which operated over 120 h with a mitigated photocurrent degradation rate ($J_{ph}/J_{ph,max}$ ~40% after the test), implying the structural stability of Pt and TiO_2 was partially maintained (Supplementary Fig. 16). The stability improvement for the Si wafer-based photocathode was limited, requiring further development on both device and hydrogel protector. Because the adhesion of as-formed gas bubbles on the flat surface increases compared with the nanostructured surface[45,46], we speculate that the bubble detachment from the flat Si surface is difficult, leading to large bubble-induced shear stress on the device surface, which deteriorates the structure stability of Pt catalyst.

Notably, the proposed device-on-top protector can be applied to not only photocathodes but also photoanodes. When the $NiFeO_x$/$BiVO_4$ photoanode was protected with 800 μm-thick 10% PAAM, the lifetime was dramatically enhanced, and continuous operation could be realized for more than 500 h (Fig. 8d; Supplementary Fig. 17 shows the thickness variation). J_{ph} fluctuation in the range ~70% to 100% of the $J_{ph,max}$ in the first ~200 h was attributable to the repeated cycles of J_{ph} reduction by bubble generation and J_{ph} recovery by bubble detachment. J_{ph} gradually decreased (200–220 h) as the O_2 gas bubbles formed inside the hydrogel protector merged and gradually expanded to a large trapped bubble. When this large bubble escaped, J_{ph} recovery was observed (350–400 h). The structural stability of the $NiFeO_x$/$BiVO_4$ photoanode was maintained even after 500 h (J_{ph}/J_o ~50%) when the hydrogel protector was used (Supplementary Fig. 18). Typically, the instability of $BiVO_4$ is associated with the dissolution of V^{5+} ions, which accelerates the photocurrent degradation. This phenomenon can be partially prevented by adding V^{5+} species to the electrolyte[47]. However, this electrolyte-tuning strategy can be used only when the metal ion precursor is soluble in the electrolyte and all the elements composing the light absorber must be considered. For example, the addition of V^{5+} can suppress only the dissolution of V^{5+} and not Bi^{3+}, according to Le Chatelier's principle. In contrast, the proposed device-on-top hydrogel protection

strategy is material independent because the protector stabilizes the dissolving ions in situ; therefore, this approach can be generically and readily adapted to various PEC devices.

Conclusions

In this study, we report a hydrogel protection strategy that can remarkably enhance the lifetime of PEC devices. Using the device-on-top design of a PAAM hydrogel protector, the lifetime of the Sb_2Se_3 photocathode could be dramatically increased from 1 h to 100 h while maintaining ~70% of initial photocurrent. Moreover, the photocurrent degradation rate gradually decreased and became nearly saturated after 100 h. We demonstrated that a well-designed hydrogel protector could impart structural stability of the Pt catalyst, preventing its agglomeration and detachment by the confinement effect, and suppress the photocorrosion of TiO_2 by stabilizing the dissolved Ti^{3+} ions inside the hydrogel via Le Chatelier's principle. In addition, the effective bubble escape via a micro gas tunnel produced in the hydrogel protector helped ensure its mechanical stability. Because the PAAM hydrogel is commonly available, easily processable and potentially applicable to photocathodes and photoanodes regardless of the electrolyte pH, the proposed hydrogel-based protection technology may provide a platform for designing stable PEC devices. Moreover, optimizing the engineering aspects of hydrogel protector, for instance, by using 3D printing and chemical functionalization[48,49], could facilitate the realization of a semi-permanent green hydrogen production system.

Methods

Materials for hydrogel coating. In this study, 1 N NaOH (98%; UN1823), acrylamide (AAM, 98%; A503181), calcium chloride ($CaCl_2$; 1098), and ethyl alcohol (99.9%; UN1170) were obtained from Duksan. Glutaraldehyde (50%; 4133-1405) and methyl alcohol (99.8%; 5558-4105) were purchased from DaeJung. Ammonium persulfate (AP, ≥98%; 248614), (3-aminopropyl)triethoxysilane (APTES, ≥98%; A3648), N,N'-methylenebisacrylamide (Bis-acrylamide, BAAM, 99%; 146072), N,N,N',N'–tetramethylethylenediamine (TEMED, 99%; T9281), agarose (A9045), gelatin from bovine skin (type B) (G9391), sodium alginate (W201502), Dulbecco's phosphate buffered saline (1× PBS; D8662), 10× PBS (59331 C), poly(ethylene glycol) diacrylate (PEGDA; molecular weight of 575; 437441) and fluorescein isothiocyanate–dextran (FITC–dextran; molecular weight of 20 kDa; FD20S) were purchased from Sigma-Aldrich. Gelatin methacrylate (GelMA) was purchased from Allevi, collagen I (354236) was purchased from Corning and 2-hydroxy-4'-(2-hydroxyethoxy)-2-methylpropiophenone (Irgacure 2959) was purchased from BASF Schweiz. A commercial water-repelling coating agent (Rain-X original water repellent, Illinois Tool Works) was purchased from a local mart.

Fabrication of Sb_2Se_3 photocathodes. Sb_2Se_3 photocathodes were fabricated on a 70 nm-thick Au-coated fluorine-doped tin oxide (FTO) glass through a spin coating and annealing process. A 0.258 g sample of $SbCl_3$ salt was dissolved in 12.19 ml 2-methoxyethanol (2ME), and 0.385 g of Se powder was dissolved in a co-solvent system of 0.45 ml thioglycolic acid (TGA) and 7.37 ml ethanolamine (EA). Two solutions were magnetically stirred at 80 °C overnight before use. Spin coating was conducted at 2,000 r.p.m. for 30 s, followed by a sequential two-step drying process at 180 °C and 300 °C for 3 min each. This cycle was repeated ten times, and subsequently, the sample was annealed at 350 °C for 20 min. Spin coating and annealing were conducted in an N_2-filled glovebox to prevent the formation of unnecessary oxide phases. Finally, post-annealing was performed at 200 °C for 30 min in air (Supplementary Note 6 presents the physical and chemical properties of as-prepared Sb_2Se_3 nanostructured film). The TiO_2 layer was immediately deposited onto the Sb_2Se_3 film through ALD (NCS Inc.), using tetrakis(dimethylamido)titanium (TDMAT) and H_2O as Ti and O sources, respectively. The evaporation and deposition temperatures were 75 °C and 150 °C, respectively. A total of 600 ALD cycles were implemented, with each cycle involving a TDMAT pulse (0.3 s) followed by 15 s of N_2 purging and an H_2O pulse of 0.2 s followed by 15 s of N_2 purging. The growth rate of TiO_2 was approximately 0.58 Å per cycle. The Pt co-catalyst was sputtered onto the TiO_2/Sb_2Se_3 electrode by using an auto sputter coater (Ted Pella) under an applied current of 10 mA for 120 s.

Surface treatment of Pt/TiO_2/Sb_2Se_3 photocathode. The surface of the Pt/TiO_2/Sb_2Se_3 photocathode was treated with NaOH, APTES and glutaraldehyde to ensure chemical bonding between the polyacrylamide hydrogel and PEC device. The 1 N NaOH and 50% glutaraldehyde solutions were diluted with deionized (DI) water to prepare 0.1 N NaOH and 0.5% glutaraldehyde solutions, respectively. The APTES solution was diluted with ethyl alcohol to prepare a 0.5% APTES solution. The prepared Pt/TiO_2/Sb_2Se_3 photocathode was dipped in a 0.1 N NaOH solution for 5 min. After retrieving the photocathode from the NaOH solution, the 0.5% APTES solution was poured onto the photocathode for 5 min. The photocathode was washed with an ethyl alcohol solution for six cycles after removing the APTES solution. Subsequently, the 0.5% glutaraldehyde solution was poured onto the photocathode for 30 min. After removing the glutaraldehyde solution from the photocathode, the photocathode was washed with DI water for six cycles and dried in an oven at 60 °C for 30 min.

Deposition of PAAM hydrogel on the photocathode. PDMS moulds were prepared by cutting a silicon rubber thin film (Elastosil 2030, Wacker) using a cutting plotter (CE6000-120, Graphtec). After cleaning the PDMS moulds with 70% ethyl alcohol and removing the dust on the moulds by using a double-sided tape, the PDMS mould was placed on the surface-treated photocathodes.

A 100% weight per volume (w/v) AAM solution was prepared by dissolving 1 g acrylamide powder in 1 ml DI water. Bis-acrylamide (2% w/v) was prepared by dissolving 20 mg bis-acrylamide powder in 1 ml DI water. The 10% AP solution was prepared by dissolving the AP powder (10 mg) in 100 µl of DI water. The pre-gel solution was prepared by mixing the acrylamide solution, bis-acrylamide solution and DI water, according to the given chart (Supplementary Table 3), with gentle pipetting and by degassing for more than 1 h. The monomer-crosslinker concentration ratio (AAM: BAAM) was 80:1.

Gelation was initiated by adding the AP and TEMED solutions to the pre-gel solution. The final concentrations of AP and TEMED were 0.05 wt.% and 0.1 wt.%, respectively. A mixture of the pre-gel solution with the AP and TEMED solutions was introduced over the photocathode surface, which was covered with the cover glass. The cover glass was immersed in a water-repellant agent (Rain-X) for 3 min before initiating gelatin to detach the solidified hydrogel from the glass. After gelation for 30 min, the cover glass and PDMS mould were carefully removed. Thereafter, the surface of the photocathode on which the hydrogel was not coated was covered with epoxy resin.

Fabrication of PEC devices for the versatility test. The solution-processed SnS photocathode was fabricated by spin coating a seed ink followed by a growth ink. The SnS seed ink was prepared by dissolving 3 mmol of $SnCl_2{\cdot}2H_2O$ (Sigma-Aldrich, 98%) and 3 mmol of S powder (Sigma-Aldrich, 99.98%) in 2 ml 2-mercaptoethanol (Sigma-Aldrich, 99%) and 8 ml ethylenediamine (Sigma-Aldrich, 99.5%). The SnS growth ink was prepared by dissolving 15 mmol of $SnCl_2{\cdot}2H_2O$ and 10 mmol of thiourea (Sigma-Aldrich, 98%) in 10 ml 2ME (Sigma-Aldrich, 99%). The SnS seed ink was spin coated onto the Au/FTO substrates at 500 r.p.m. for 5 s and 3,500 r.p.m. for 25 s, followed by instant annealing on a hot plate at 180 °C and 300 °C for 3 min in a N_2-filled glovebox. After sufficient cooling, the spin coating of SnS growth ink was conducted three times following an identical cycle as that of seed ink. Subsequently, as-prepared SnS samples were treated in a bath solution mixed of $CdSO_4$ (Sigma-Aldrich, 99.99%), thiourea, NH_4OH (Duksan, 28 wt.%) and DI water at 55 °C for 3 min to deposit an *n*-type CdS overlayer. After the CdS deposition, TiO_2 layer was deposited via ALD, and Pt co-catalyst was sputtered identically as the Sb_2Se_3 photocathode.

For Si photocathodes, the *p*-Si wafers (Boron doping, 10–30 Ω·cm, single-side polished) were cut into 2 × 1 cm pieces, which were then cleaned through ultrasonication for 10 min each in acetone, soapy water (Deconex), DI water and ethanol. This was followed by 10 min of ultrasonication in a $H_2O/H_2O_2/NH_4OH$ (5:1:1) solution, 10 min of that in a $H_2O/H_2O_2/HCl$ 5:1:1 solution, and 1 min of that in a 2% HF solution. Samples were then rinsed with water, dried in a N_2 stream and immediately used for the next step. The TiO_2 layer was deposited with the same ALD recipe as mentioned above but using 920 cycles, which yielded ~ 55 nm of thickness. After sputtering the Pt catalyst for 120 s, another TiO_2 overlayer (ALD 50 cycle, ~3 nm) was deposited to enhance the Pt adhesion.

To prepare the $BiVO_4$ photoanode, first, SnO_2 bottom layer was deposited on FTO substrate via the sol–gel method. A 50 mmol $SnCl_2{\cdot}2H_2O$ (Sigma-Aldrich, 98%) was dissolved in 5 ml isopropyl alcohol, which was spin coated on FTO at 2,000 r.p.m. for 30 s and annealed at 500 °C for 1 h under ambient air. For the $BiVO_4$ molecular ink, 1 M $Bi(NO_3)_3{\cdot}5H_2O$ (Sigma-Aldrich, 98%) in acetic acid (Duksan Pure Chemicals) and 0.15 M $VO(acac)_2$ (Sigma-Aldrich, 98%) in methanol (Duksan Pure Chemicals) were mixed with a Bi:V stoichiometric ratio of 1:1. The $BiVO_4$ ink was spin coated on the SnO_2/FTO substrate at 1,500 r.p.m. for 20 s, followed by annealing on a hot plate at 400 °C for 7 min under ambient air. The spin coating and annealing processes were performed seven times, followed by the final annealing at 480 °C for 30 min in a box furnace (ramping rate = 10 °C per min). For the $NiFeO_x$ co-catalyst, 60 mg $Fe(SO_4)_2{\cdot}7H_2O$ (Sigma-Aldrich, 99%) and 20 mg $Ni(SO_4)_2{\cdot}6H_2O$ (Sigma-Aldrich, 99%) were dissolved in 200 ml of 0.5 M $KHCO_3$ (Ar purging for 30 min before use) solution. For the deposition, LSV from −0.3 to 0.5 $V_{Ag/AgCl}$ was performed 18 times under illumination (AM 1.5 G, 100 mW cm^{-2}) with a 5 s pretreatment at −0.3 $V_{Ag/AgCl}$ for each sweep. After the deposition, the $NiFeO_x/BiVO_4$ photoanode was washed with DI water and dried at 80 °C for 30 min.

These photoelectrodes were used as reference devices without the hydrogel protector. To fabricate the 10% PAAM device-on-top protector, surface treatment and gelation process were conducted as in the case of the Sb_2Se_3 photocathodes.

Finally, the surface of the photoelectrodes on which the hydrogel was not coated was covered with epoxy resin. The neutral (pH 7) and basic (pH 9) electrolytes were 0.5 M potassium phosphate (KPi) buffer with 0.5 M Na_2SO_3 and 1.0 M potassium borate (KBi) buffer, respectively.

PEC characterization. The characterizations of the photoelectrode, including LSV and chronoamperometry analyses, were conducted using a typical three-electrode system with a Ag/AgCl/KCl (saturated) reference electrode and Pt counter electrode. The three electrodes were submerged in a 0.1 M aqueous H_2SO_4 (pH ~1) solution, and the simulated solar-light illumination (AM 1.5 G, Newport Corporation) was used for all the measurements. The calibration of the one-sun level was performed using a 2 × 2 cm (ref. [2]) calibrated solar cell made of monocrystalline silicon (Newport Corporation). The IPCE measurement was conducted using an electrochemical workstation (Zennium, Zahner) and a potentiostat (PP211, Zahner) under monochromatic light irradiation at 0 V versus RHE.

Material characterization. The optical transmittance and reflectance spectra were recorded at room temperature by using a UV–vis spectrophotometer (V-670, JASCO) equipped with an integrating sphere. The surface morphology evolution of the Sb_2Se_3 photocathodes was analysed through FE-SEM (JSM 7001 F, JEOL Ltd.). The focused ion beam technique was used to prepare electron-transparent foils from the selected Sb_2Se_3 photocathodes, and their microstructures were analysed using TEM-EDS (Talos F200X, FEI) at an acceleration voltage of 200 kV.

Time-lapse and high-speed imaging of the bubbles generated on a PEC device. Time-lapse imaging and high-speed imaging of the bubbles were performed using a digital single-lens reflex (DSLR) camera (D5300, Nikon) and high-speed camera (C320, Vision Research), respectively. The DSLR and high-speed cameras were equipped with a 2× teleconverter (TELEPLUS MC7 AF 2× DGX, Kenko) and 105 mm F2.8 macro lens (Nikon). Images were captured based on the light illumination for the PEC operation without any additional light source.

Characterization of the physical properties of the hydrogel. The volume fraction of the hydrogel was evaluated using a gravimetric method. The hydrogel samples were dried for 3 d in a dry oven at 60 °C. The weights of the samples before and after drying were measured using a precision balance (MS104S, Mettler Toledo). The volume fraction of the hydrogel, φ, was calculated as

$$\varphi = \frac{m_p v_p}{m_p v_p + (m_h - m_p) v_w}$$

where m_p, m_h, v_p and v_w represent the masses of dried and hydrated hydrogels and specific volumes of a polymer (0.7 $cm^3 g^{-1}$) and DI water (1.0 $cm^3 g^{-1}$), respectively[32,50]. The volumetric water content φ_p was calculated as

$$\varphi_p = 1 - \varphi$$

The apparent pore size of the hydrogel r_p was calculated as

$$r_p = \frac{r_s}{1 - \sqrt{\frac{1}{1-\varphi} K}}$$

where K and r_s represent the partition coefficient and radius, respectively, of the solute in the hydrogel. In particular, 20 kDa FITC–dextran with a radius of 3 nm (ref. [51]) was used as a solute to analyse the apparent pore size of the hydrogel. Assuming that the fluorescence intensity of the FITC–dextran was linearly proportional to the concentration of the FITC–dextran in the solution, the partition coefficient K could be calculated as

$K = \frac{c_{gel}}{c_{sol}} = \frac{I_{gel}}{I_{sol}}$ where c_{gel}, c_{sol}, I_{gel} and I_{gel} are the concentrations of the FITC–dextran in the hydrogel and solution and intensities of the FITC–dextran in the hydrogel and solution, respectively[32]. The fluorescence intensity of the FITC–dextran was measured using the fluorescent image obtained using an epifluorescence microscope (Ni-U, Nikon) with a charge-coupled device (CCD) camera (DS-Q1Mc, Nikon). Fluorescent images of the 20 kDa FITC–dextran in the hydrogel were obtained after immersing the hydrogel samples in a 1.0 mg ml^{-1} FITC–dextran solution for 24 h.

The chemical inertness of the hydrogel samples against the acidic environment was investigated by comparing the shape of the hydrogel after gelation and immersion in a 0.1 M sulfuric acid solution for 24 h. Two 1.2 mm-thick PDMS spacers were placed on the slide glass and the water repellent-coated glass substrate was placed on the PDMS spacers. The hydrogel solution samples were injected between the slide glass and water repellent-coated glass substrate. After gelation, the cover glass was detached, and the 1.2 mm-thick hydrogel samples were cut using a 4 mm-diameter biopsy punch. The prepared hydrogel samples were immersed in a 0.1 M sulfuric acid solution for 24 h. Thereafter, photographs of the hydrogel samples were captured using a stereomicroscope (SMZ 745 T, Nikon) and CCD camera (DS-Qi1Mc, Nikon). Agarose, alginate, collagen, gelatin, GelMA and PEGDA hydrogel samples were prepared considering the specifications listed in Supplementary Tables 4–8.

A custom-made indenter composed of a load cell (GS0-10, Transducer Techniques), motor stage (SM2-0803-3S and SZ-0604-3S, Science town) and microscope (AM4113, AnMo Electronics Corporation)[52] were used to estimate the mechanical properties of PAAM. Cylindrical PAAM hydrogel samples with a thickness of 1.2 mm and diameter in the range of 2.5–3.5 mm were used in the indentation test. Indentations were performed using a cylindrical stainless steel tip with a diameter of 5 mm. The depth and speed of the indentation of the samples were 75 μm and 2.5 μm s^{-1}, respectively. The indentation stress was estimated by dividing the applied force by the cross-sectional area of the hydrogel sample. The indentation strain was estimated as the ratio of the decrease in the sample height during indentation to the original height. The Young's modulus of a sample was calculated from the slope of the stress–strain curve assuming the following linear relationship:

$E = \frac{\sigma}{\epsilon}$, where E is the Young's modulus, σ is the applied stress and ϵ is the strain[53].

Simulation of bubble expansion in a hydrogel layer. To investigate the stress distribution in the hydrogel layer by bubble expansion, we developed a computational model based on the finite element method and using Abaqus FEA software (Dassault Systèmes). The three-dimensional axisymmetric computational model included a hydrogel layer and hemispherical cavity of the bubble. The bubble expansion was simulated by the displacement of the nodes of the hemispherical cavity. The bubble was expanded from a radius of 0.1 R to R, where R denotes the final radius of the expanded bubble. To investigate the effect of the hydrogel thickness on the stress distribution inside the hydrogel layer, the thickness of the hydrogel h was set as R, 2 R, and 10 R. The radius of the axisymmetric model was 10 R. The Young's modulus of the hydrogel in the model was 10 kPa, similar to that of 10% PAAM. The mesh of the model was established using four-node bilinear quadrilateral reduced elements (CAX4R).

Data availability

The authors declare that all data supporting the findings of this study are available within the paper and its Supplementary Information. Source data are provided with this paper.

Received: 21 June 2021; Accepted: 4 May 2022;
Published online: 9 June 2022

References

1. Lewis, N. S. Research opportunities to advance solar energy utilization. *Science* **351**, aad1920 (2016).
2. Kim, J. H., Hansora, D., Sharma, P., Jang, J.-W. & Lee, J. S. Toward practical solar hydrogen production—an artificial photosynthetic leaf-to-farm challenge. *Chem. Soc. Rev.* **48**, 1908–1971 (2019).
3. Ardo, S. et al. Pathways to electrochemical solar-hydrogen technologies. *Energy Environ. Sci.* **11**, 2768–2783 (2018).
4. Chen, S. & Wang, L.-W. Thermodynamic oxidation and reduction potentials of photocatalytic semiconductors in aqueous solution. *Chem. Mater.* **24**, 3659–3666 (2012).
5. Bae, D., Seger, B., Vesborg, P. C. K., Hansen, O. & Chorkendorff, I. Strategies for stable water splitting via protected photoelectrodes. *Chem. Soc. Rev.* **46**, 1933–1954 (2017).
6. Yang, W., Prabhakar, R. R., Tan, J., Tilley, S. D. & Moon, J. Strategies for enhancing the photocurrent, photovoltage, and stability of photoelectrodes for photoelectrochemical water splitting. *Chem. Soc. Rev.* **48**, 4979–5015 (2019).
7. Tan, J. et al. Fullerene as a photoelectron transfer promoter enabling stable TiO_2-protected Sb_2Se_3 photocathodes for photo-electrochemical water splitting. *Adv. Energy Mater.* **9**, 1900179 (2019).
8. Yang, W. et al. Benchmark performance of low-cost Sb_2Se_3 photocathodes for unassisted solar overall water splitting. *Nat. Commun.* **11**, 861 (2020).
9. Paracchino, A., Laporte, V., Sivula, K., Grätzel, M. & Thimsen, E. Highly active oxide photocathode for photoelectrochemical water reduction. *Nat. Mater.* **10**, 456–461 (2011).
10. Rojas, H. C. et al. Polymer-based photocathodes with a solution-processable cuprous iodide anode layer and a polyethyleneimine protective coating. *Energy Environ. Sci.* **9**, 3710–3723 (2016).
11. Yang, W. et al. Adjusting the anisotropy of 1D Sb_2Se_3 nanostructures for highly efficient photoelectrochemical water splitting. *Adv. Energy Mater.* **8**, 1702888 (2018).
12. Rovelli, L., Tilley, S. D. & Sivula, K. Optimization and stabilization of electrodeposited Cu_2ZnSnS_4 photocathodes for solar water reduction. *ACS Appl. Mater. Interfaces* **5**, 8018–8024 (2013).
13. Koo, B. et al. Reduced graphene oxide as a catalyst binder: greatly enhanced photoelectrochemical stability of Cu(In,Ga)Se_2 photocathode for solar water splitting. *Adv. Funct. Mater.* **28**, 1705136 (2018).
14. Tilley, S. D., Schreier, M., Azevedo, J., Stefik, M. & Graetzel, M. Ruthenium oxide hydrogen evolution catalysis on composite cuprous oxide water-splitting photocathodes. *Adv. Funct. Mater.* **24**, 303–311 (2014).

15. Morales-Guio, C. G., Tilley, S. D., Vrubel, H., Grätzel, M. & Hu, X. Hydrogen evolution from a copper(I) oxide photocathode coated with an amorphous molybdenum sulphide catalyst. *Nat. Commun.* **5**, 3059 (2014).
16. Labrador, N. Y. et al. Enhanced performance of Si MIS photocathodes containing oxide-coated nanoparticle electrocatalysts. *Nano Lett.* **16**, 6452–6459 (2016).
17. Vanka, S. et al. InGaN/Si double-junction photocathode for unassisted solar water splitting. *ACS Energy Lett.* **5**, 3741–3751 (2020).
18. Yin, Z., Fan, R., Huang, G. & Shen, M. 11.5% efficiency of TiO_2 protected and Pt catalyzed n^+np^+-Si photocathodes for photoelectrochemical water splitting: manipulating the Pt distribution and Pt/Si contact. *Chem. Commun.* **54**, 543–546 (2018).
19. Tilley, S. D. Recent advances and emerging trends in photo-electrochemical solar energy conversion. *Adv. Energy Mater.* **9**, 1802877 (2019).
20. Croce, R. & van Amerongen, H. Natural strategies for photosynthetic light harvesting. *Nat. Chem. Biol.* **10**, 492–501 (2014).
21. Show, K.-Y. et al. Hydrogen production from algal biomass—advances, challenges and prospects. *Bioresour. Technol.* **257**, 290–300 (2018).
22. Le Bail, A., Billoud, B., Le Panse, S., Chenivesse, S. & Charrier, B. ETOILE regulates developmental patterning in the filamentous brown alga *Ectocarpus siliculosus*. *Plant Cell* **23**, 1666–1678 (2011).
23. Rabillé, H. et al. Alginates along the filament of the brown alga *Ectocarpus* help cells cope with stress. *Sci. Rep.* **9**, 12956 (2019).
24. Tesson, B. & Charrier, B. Brown algal morphogenesis: atomic force microscopy as a tool to study the role of mechanical forces. *Front. Plant Sci.* **5**, 471 (2014).
25. Domozych, D. S., Kozel, L. & Palacio-Lopez, K. The effects of osmotic stress on the cell wall–plasma membrane domains of the unicellular streptophyte, *Penium margaritaceum*. *Protoplasma* **258**, 1231–1249 (2021).
26. Su, X. & Chen, B. Transparent, UV-proof and mechanically strong montmorillonite/alginate/Ca^{2+} nanocomposite hydrogel films with solvent sensitivity. *Appl. Clay Sci.* **165**, 223–233 (2018).
27. Ahmad Raus, R., Wan Nawawi, W. M. F. & Nasaruddin, R. R. Alginate and alginate composites for biomedical applications. *Asian J. Pharm. Sci.* **16**, 280–306 (2021).
28. Jeon, D. et al. Superaerophobic hydrogels for enhanced electrochemical and photoelectrochemical hydrogen production. *Sci. Adv.* **6**, eaaz3944 (2020).
29. Wang, L. et al. Stable 6%-efficient Sb_2Se_3 solar cells with a ZnO buffer layer. *Nat. Energy* **2**, 17046 (2017).
30. Li, Z. et al. 9.2%-efficient core-shell structured antimony selenide nanorod array solar cells. *Nat. Commun.* **10**, 125 (2019).
31. Chen, C. et al. Characterization of basic physical properties of Sb_2Se_3 and its relevance for photovoltaics. *Front. Optoelectron.* **10**, 18–30 (2017).
32. Tong, J. & Anderson, J. L. Partitioning and diffusion of proteins and linear polymers in polyacrylamide gels. *Biophys. J.* **70**, 1505–1513 (1996).
33. Fischer, R. S., Myers, K. A., Gardel, M. L. & Waterman, C. M. Stiffness-controlled three-dimensional extracellular matrices for high-resolution imaging of cell behavior. *Nat. Protoc.* **7**, 2056–2066 (2012).
34. Huang, C. & Guo, Z. The wettability of gas bubbles: from macro behavior to nano structures to applications. *Nanoscale* **10**, 19659–19672 (2018).
35. Takahashi, R. et al. Tough particle-based double network hydrogels for functional solid surface coatings. *Adv. Mater. Interfaces* **5**, 1801018 (2018).
36. Pan, L. et al. Boosting the performance of Cu_2O photocathodes for unassisted solar water splitting devices. *Nat. Catal.* **1**, 412–420 (2018).
37. Paracchino, A. et al. Ultrathin films on copper(I) oxide water splitting photocathodes: a study on performance and stability. *Energy Environ. Sci.* **5**, 8673–8681 (2012).
38. Paciok, P., Schalenbach, M., Carmo, M. & Stolten, D. On the mobility of carbon-supported platinum nanoparticles towards unveiling cathode degradation in water electrolysis. *J. Power Sources* **365**, 53–60 (2017).
39. Galeano, C. et al. Toward highly stable electrocatalysts via nanoparticle pore confinement. *J. Am. Chem. Soc.* **134**, 20457–20465 (2012).
40. Wen, J. H. et al. Interplay of matrix stiffness and protein tethering in stem cell differentiation. *Nat. Mater.* **13**, 979–987 (2014).
41. Shiva, A. H., Teasdale, P. R., Bennett, W. W. & Welsh, D. T. A systematic determination of diffusion coefficients of trace elements in open and restricted diffusive layers used by the diffusive gradients in a thin film technique. *Anal. Chim. Acta* **888**, 146–154 (2015).
42. Scheiner, S. & Hellmich, C. Stable pitting corrosion of stainless steel as diffusion-controlled dissolution process with a sharp moving electrode boundary. *Corros. Sci.* **49**, 319–346 (2007).
43. Kundu, S. & Crosby, A. J. Cavitation and fracture behavior of polyacrylamide hydrogels. *Soft Matter* **5**, 3963–3968 (2009).
44. Lai, Y. & Hu, Y. Probing the swelling-dependent mechanical and transport properties of polyacrylamide hydrogels through AFM-based dynamic nanoindentation. *Soft Matter* **14**, 2619–2627 (2018).
45. Angulo, A., Linde, P. V. D., Gardeniers, H., Modestino, M. & Rivas, D. F. Influence of bubbles on the energy conversion efficiency of electrochemical reactors. *Joule* **4**, 555–579 (2020).
46. Lu, Z. et al. Ultrahigh hydrogen evolution performance of under-water "superaerophobic" MoS_2 nanostructured electrodes. *Adv. Mater.* **26**, 2683–2687 (2014).
47. Lee, D. K. & Choi, K.-S. Enhancing long-term photostability of $BiVO_4$ photoanodes for solar water splitting by tuning electrolyte composition. *Nat. Energy* **3**, 53 (2018).
48. Koons, G. L., Diba, M. & Mikos, A. G. Materials design for bone-tissue engineering. *Nat. Rev. Mater.* **5**, 584–603 (2020).
49. Shi, Y., Ilic, O., Atwater, H. A. & Greer, J. R. All-day fresh water harvesting by microstructured hydrogel membranes. *Nat. Commun.* **12**, 2797 (2021).
50. Lewus, R. K. & Carta, G. Protein diffusion in charged polyacrylamide gels. *Vis. Anal. J. Chromatogr. A* **865**, 155–168 (1999).
51. Branco, M. C., Pochan, D. J., Wagner, N. J. & Schneider, J. P. Macromolecular diffusion and release from self-assembled beta-hairpin peptide hydrogels. *Biomaterials* **30**, 1339–1347 (2009).
52. Chang, S. et al. Multi-scale characterization of surface-crosslinked superabsorbent polymer hydrogel spheres. *Polymer* **145**, 174–183 (2018).
53. Choi, S. et al. Osteoconductive hybrid hyaluronic acid hydrogel patch for effective bone formation. *J. Control. Release* **327**, 571–583 (2020).

Acknowledgements

This work was supported by the National Research Foundation (NRF) of Korea grant (numbers 2021R1A3B1068920 (J.M.), 2021M3H4A1A03049662 (J.M.), 2021R1A2C2009070 (Hyungsuk Lee) and 2021R1I1A1A01060058 (J.T.)), funded by the Ministry of Science and ICT. This research was also supported by the Yonsei Signature Research Cluster Program of 2021 (2021–22-0002, J.M.). We thank M. Na for TEM analysis.

Author contributions

J.T., B.K., Hyungsuk Lee, and J.M. conceived the project idea. J.T. and B.K. conducted experiments, analysed the data and drafted the manuscript. K.K. conducted the experiments and analysed the data. D.K. conducted a simulation-based analysis. Hyungsoo Lee, S.M. and G.J. supported the experiments. Hyungsuk Lee and J.M. supervised the project, directed the research and contributed to writing the manuscript.

Competing interests

The authors declare no competing interests.

Additional information

Supplementary information The online version contains supplementary material available at https://doi.org/10.1038/s41560-022-01042-5.

Correspondence and requests for materials should be addressed to Hyungsuk Lee or Jooho Moon.

Peer review information *Nature Energy* thanks the anonymous reviewers for their contribution to the peer review of this work.